

Annual Review of Fluid Mechanics

Subglacial Plumes

Ian J. Hewitt

Mathematical Institute, University of Oxford, Oxford OX2 6GG, United Kingdom;
email: hewitt@maths.ox.ac.uk

Annu. Rev. Fluid Mech. 2020.52:145-169. Downloaded from www.annualreviews.org
Access provided by Boise State University on 10/08/21. For personal use only.

Annu. Rev. Fluid Mech. 2020. 52:145–69

First published as a Review in Advance on
August 5, 2019

The *Annual Review of Fluid Mechanics* is online at
fluid.annualreviews.org

<https://doi.org/10.1146/annurev-fluid-010719-060252>

Copyright © 2020 by Annual Reviews.
All rights reserved

**ANNUAL
REVIEWS CONNECT**

www.annualreviews.org

- Download figures
- Navigate cited references
- Keyword search
- Explore related articles
- Share via email or social media

Keywords

plumes, ice, ocean, melting, cryosphere, climate

Abstract

Buoyant plumes form when glacial ice melts directly into the ocean or when subglacial meltwater is discharged to the ocean at depth. They play a key role in regulating heat transport from the ocean to the ice front, and in exporting glacial meltwater to the open ocean. This review summarizes current understanding of the dynamics of these plumes, focusing on theoretical developments and their predictions for submarine melt rates. These predictions are sensitive to ocean temperature, the magnitude and spatial distribution of subglacial discharge, the ambient stratification, and, in the case of sub-ice shelf plumes, the geometry of the ice shelf. However, current understanding relies heavily on parameterizations of melting and entrainment, for which there is little in the way of validation. New observational and experimental constraints are needed to elucidate the structure of the plumes and lend greater confidence to the models.

Submarine melting:
melting from an ice
front or ice shelf

Tidewater glacier:
a glacier that
terminates in the
ocean

Grounding line: the
boundary between a
grounded ice sheet and
floating ice shelf

Ice shelf cavity:
the part of the ocean
beneath a floating ice
shelf

1. INTRODUCTION

A large fraction of the meltwater from Earth's ice sheets is discharged directly into the ocean at depth. It initiates buoyant plumes that rise up the ice–ocean interface, mixing with ambient ocean water. The dynamics of these plumes are important for regulating the heat transfer that drives submarine melting, and in controlling the depth at which glacial meltwater is exported to the open ocean. They are therefore a crucial factor in both the ice sheet response to ocean warming (Joughin et al. 2012) and the ocean response to ice sheet melting (Straneo & Heimbach 2013).

Plumes form both at the near-vertical front of tidewater glaciers and beneath relatively shallow-sloping ice shelves (**Figure 1**). The former are typical of the Greenland ice sheet, Alaska, and Svalbard, while the latter are typical of the margin of the Antarctic ice sheet. At tidewater glaciers, plume-driven melting affects the shape of the front and so also plays a role in iceberg calving. Beneath ice shelves, both melting and freezing [due to the ice pump (Lewis & Perkin 1986)] affect the shape of the ice shelf, which has an important buttressing effect on the location of the grounding line and the ice flow across it.

The ocean water adjacent to the ice sheets is typically within a few degrees of the freezing point, but is a mix of waters with different origins and properties. In Greenland, outlet glaciers terminate in narrow fjords that are typically hundreds of meters deep. The fjord water is often stratified, with relatively cold and fresh Polar Water overlying warmer and saltier Atlantic Water (Straneo et al. 2012). The plumes themselves play a role in controlling the circulation in the fjords and the exchange of water with the continental shelf (Straneo & Cenedese 2015). In Antarctica, several water masses enter beneath the ice shelves (Jacobs et al. 1992, Jenkins et al. 2016). These include Shelf Water, which is close to the surface freezing point and has high salinity due to sea ice formation; Antarctic Surface Water, which is also cold but less dense; and Circumpolar Deep Water, which is relatively warm and salty but is only able to intrude into ice shelf cavities in certain locations due to the topography of the continental shelf and wind forcing.

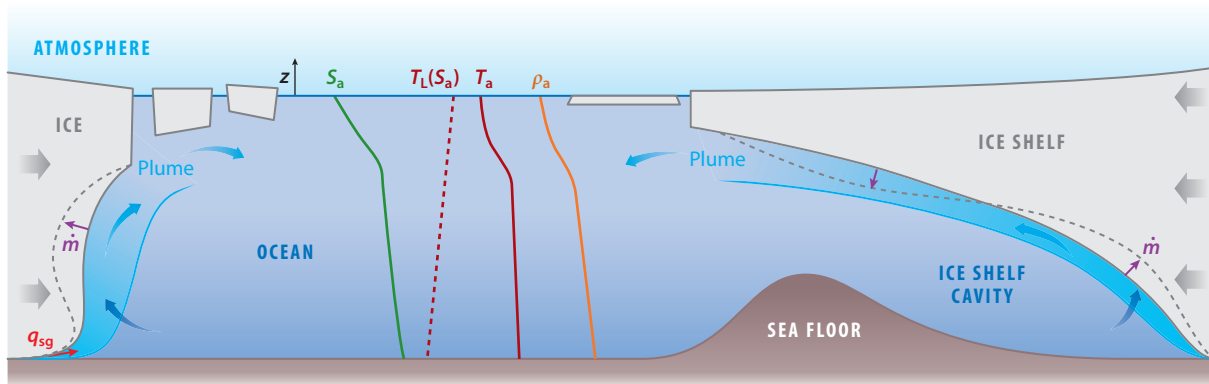


Figure 1

Plumes occur at the front of tidewater glaciers and beneath floating ice shelves. Subglacial discharge q_{sg} (red arrow) and submarine melting \dot{m} (purple arrows) produce buoyant water that rises up the ice front, entraining warmer ocean water. Typical profiles of ambient salinity S_a , temperature T_a , and density ρ_a , as well as liquidus $T_L(S_a)$, are shown. The plume controls the melt rate and hence the shape of the ice–ocean interface. It can reach a level of neutral buoyancy and separate from the ice front, controlling the depth at which glacially modified water is exported to the open ocean. Decompression raises the freezing point so the plume can become supercooled, resulting in freeze-on of marine ice to the ice shelf base (the ice pump) and creating cold waters that subsequently sink to produce Antarctic Bottom Water.

Subglacial plumes have similarities with turbulent plumes in other contexts, but they also have some distinguishing features that make them fascinating in their own right. They are wall-bounded flows in a stratified environment, initiated by a line or point source of subglacial discharge, and sustained by a distributed source of buoyancy from submarine melting. Importantly, the boundary is reactive, so both its shape and the distributed buoyancy source are coupled to the dynamics of the plume.

The questions of the rise height of a plume and the intrusion at a depth of neutral buoyancy are related to work on thermals and volcanic plumes (Woods 2010). The wall-bounded nature of the flow and to some extent the reactive boundary have similarities with self-accelerating turbidity currents (Parker et al. 1986, Meiburg & Kneller 2010). Some plumes are also large enough to be affected by rotation, and they bear some resemblance to katabatic winds (Van den Broeke & Van Lipzig 2003). Related dynamics also occur in the context of ventilation (Cooper & Hunt 2010).

This review focuses primarily on theoretical descriptions of subglacial plumes, which have built on the classical theory of plumes and gravity currents (Morton et al. 1956, Turner 1979). We touch on laboratory experiments, field observations, and attempts to include plume dynamics in larger-scale numerical models.

2. BACKGROUND

2.1. Equation of State

At conditions relevant to the polar oceans, the density of sea water increases with salinity S and decreases weakly with temperature T (Figure 2a). A linear approximation is usually adopted that is appropriate for salinities around 35 g/kg and temperatures around 0°C. The normalized

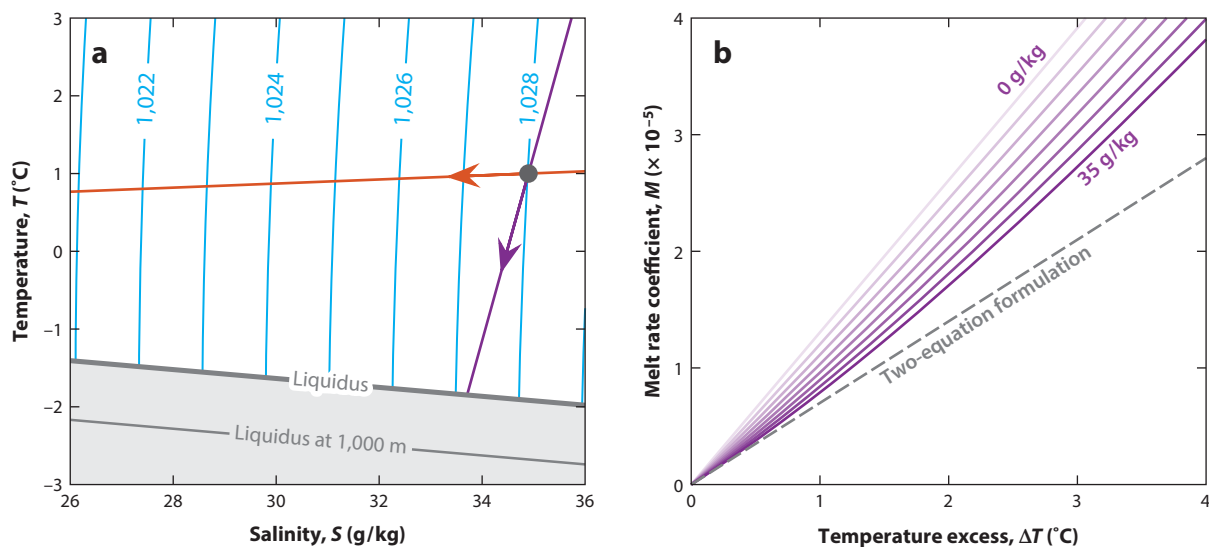


Figure 2

(a) Density contours of sea water in conditions relevant to the polar oceans at atmospheric pressure. The addition of fresh water causes mixing along the red line. The addition of ice at its freezing point causes melting and consequent mixing along the purple line. Both lead to a decrease in density. (b) Melt rate coefficient, $M = \dot{m}/U$, as a function of thermal driving, $\Delta T = T - T_L(S)$, in the three-equation formulation, for salinities in the range from 0 to 35 g/kg (at 5-g/kg intervals). The dashed line shows the two-equation formulation (Equation 11). Parameter values are from Table 1.

Table 1 Typical parameter values

Parameter	Symbol	Value
Haline contraction coefficient	β_S	7.86×10^{-4}
Thermal expansion coefficient	β_T	$3.87 \times 10^{-5} \text{ }^\circ\text{C}^{-1}$
Reference temperature	T_o	$8.32 \times 10^{-2} \text{ }^\circ\text{C}$
Liquidus slope with depth	λ	$7.61 \times 10^{-4} \text{ }^\circ\text{C/m}$
Liquidus slope with salinity	Γ	$5.73 \times 10^{-2} \text{ }^\circ\text{C}$
Gravitational acceleration	g	9.8 m/s^2
Specific heat capacity of water	c	$3,974 \text{ J}\cdot\text{kg}^{-1}\text{ }^\circ\text{C}$
Specific heat capacity of ice	c_i	$2,009 \text{ J}\cdot\text{kg}^{-1}\text{ }^\circ\text{C}$
Latent heat	L	$3.35 \times 10^5 \text{ J/kg}$
Drag coefficient	C_d	2.5×10^{-3}
Thermal Stanton number	$St_T = C_d^{1/2} \Gamma_T$	1.1×10^{-3}
Haline Stanton number	$St_S = C_d^{1/2} \Gamma_S$	3.1×10^{-5}
Composite Stanton number	$St = C_d^{1/2} \Gamma_{TS}$	5.9×10^{-4}
Entrainment coefficient	E_0	3.6×10^{-2}
Cylindrical entrainment coefficient	α	0.1

Values of Stanton numbers are those suggested by Jenkins et al. (2010), which have been widely adopted. Drag coefficient and entrainment rate are also quite uncertain; these represent commonly used values.

density deficit, or buoyancy, with respect to ambient salinity S_a and temperature T_a , is

$$\frac{\Delta\rho}{\rho_o} = \frac{\rho_a - \rho}{\rho_o} = \beta_S(S_a - S) - \beta_T(T_a - T), \quad 1.$$

where ρ_o is a reference density, β_S is the haline contraction coefficient, and β_T is the thermal expansion coefficient. Note that $g' = \Delta\rho g/\rho_o$ is the reduced gravity often used to describe buoyancy, but we use $\Delta\rho$ for greater consistency with the literature on subglacial plumes. The relevant water masses are within a few degrees of the freezing point, whereas salinity can vary considerably, so it is salinity that exerts primary control on the buoyancy.

The freezing temperature (the liquidus) depends on salinity and pressure and is usually expressed as a linear function,

$$T_L(S, z) = T_o + \lambda z - \Gamma S, \quad 2.$$

where T_o is a reference, λ is the slope of the freeing point with depth (z , with positive values in the upward direction), and Γ is the dependence on salinity (see **Table 1**). We suppress the argument z and write $T_L(S)$, but note that the depth dependence is significant (the freezing point is depressed by 0.76°C at 1,000 m depth). A useful concept is the temperature excess, or thermal driving, defined as the difference between the temperature and the local freezing point,

$$\Delta T = T - T_L(S). \quad 3.$$

(To avoid confusion, we should clarify that the use of “ Δ ” here is different from that in Equation 1: The term $\Delta\rho$ denotes difference from ambient conditions, while ΔT denotes difference from the local liquidus; Δ is never used as a quantity on its own.)

Density deficit:

$\Delta\rho = \rho_a - \rho$, the difference from ambient density, sometimes called buoyancy

Temperature excess:

$\Delta T = T - T_L(S)$, the temperature above the local freezing point, also called thermal driving

2.2. Buoyancy Sources

Two distinct sources of buoyancy are important: subglacial discharge and submarine melt. Subglacial discharge is meltwater that is sourced from the surface or base of the grounded ice sheet (see the sidebar titled Subglacial Discharge). It is essentially fresh and emerges close to the pressure-dependent freezing point. It is therefore considerably lighter than the ambient water, with density deficit

$$\Delta\rho_{\text{sg}}/\rho_o = \beta_S(S_a - S_i) - \beta_T[T_a - T_L(S_i)] \approx 0.028, \quad 4.$$

SUBGLACIAL DISCHARGE

Subglacial discharge is meltwater produced at the base of a glacier by geothermal or frictional heating or meltwater from the glacier surface that is routed to the base through crevasses and moulins. It is possible that some discharge emerges at intermediate depths through englacial channels, but most is thought to travel along the interface between ice and substrate, emerging at the base of the ice front or grounding line.

Distribution

Subglacial water flow is driven by a hydraulic potential, controlled primarily by ice surface elevation (Cuffey & Paterson 2010, Fountain & Walder 1998). It follows roughly the same flow lines as the ice. Some of the flow may be distributed widely across the bed, in permeable sediments or linked cavities that form as ice slides over its substrate. However, much of the flow is concentrated in tunnels—Röthlisberger channels—incised upward into the ice. These tunnels are enlarged through dissipation-driven melting of their walls, counteracted by viscous creep when the subglacial water pressure is less than the pressure in the ice. The partitioning of subglacial discharge between distributed and point sources is largely unknown. Observations of isolated plumes (e.g., Mankoff et al. 2016) and localized undercutting (e.g., Fried et al. 2015) indicate that a substantial part of it is channelized, at least in places with large discharge, but the extent of distributed discharge across the rest of the ice front is still uncertain.

Magnitude

Direct measurement of subglacial discharge is challenging, so it is usually estimated based on upstream sources. The order of magnitude of basal melting beneath grounded ice sheets is 1–10 mm/year. Over a flow line distance of, say, 300 km, this gives a typical discharge on the order of 10^{-5} – 10^{-4} m²/s per unit width, not accounting for convergence from a wider catchment. Surface melting occurs at typical rates of 1–10 m/year over distances on the order of 30 km, giving larger fluxes on the order of 10^{-3} – 10^{-2} m²/s averaged over the year. Integrating over catchment basins, estimates of summer discharge beneath Greenland glaciers are on the order of 10–1,000 m³/s, entering fjords of width 1–10 km (e.g., Carroll et al. 2016).

Timing

In Greenland there is a strong seasonal cycle of surface melting that dominates subglacial discharge. There can be a time lag of days to weeks between melting and discharge due to temporary storage in supraglacial lakes and the subglacial drainage system, especially early in summer when the drainage system is less developed (e.g., Chandler et al. 2013). In Antarctica, where discharge is sourced from basal melting, there is no reason to expect a seasonal signal. Filling and drainage of subglacial lakes (with a timescale of months to years) have shown that drainage is nevertheless unsteady, and episodic discharge events are likely (e.g., Fricker et al. 2007, Stearns et al. 2008). Tidal modulations are also likely since tides control the hydraulic potential close to the grounding line.

Modified latent heat:
the energy $\tilde{L} = L + c_i[T_L(S_i) - T_i]$ accounts for the latent heat as well as warming ice at temperature T_i to its melting point

for $S_a = 35$ g/kg and $T_a = 0^\circ\text{C}$ (the value changes little over a range of ambient conditions and can essentially be treated as constant). For notational convenience, we have introduced the salinity of the ice (and subglacial discharge), $S_i \approx 0$. Adding such water to cold ocean water causes mixing along an almost horizontal line in T - S space (**Figure 2a**).

Submarine melt occurs directly into the ocean. This similarly provides a source of fresh water, but because the energy required for the phase change must come from the ocean itself, it also causes substantial cooling. Accounting for the latent heat L plus the energy required to first warm the ice from temperature T_i to its melting point, we can take this meltwater to have an effective temperature excess of

$$\Delta T_i^{\text{ef}} = -\frac{L + c_i[T_L(S_i) - T_i]}{c} = -\frac{\tilde{L}}{c} \quad 5.$$

and an effective meltwater temperature of $T_i^{\text{ef}} = T_L(S_i) + \Delta T_i^{\text{ef}}$. Here c_i and c are the specific heat capacity of ice and water, respectively. The quantity ΔT_i^{ef} is a proxy for the modified latent heat \tilde{L} and takes values of $\lesssim -84^\circ\text{C}$. Submarine melting therefore causes mixing along a steeper line in **Figure 2a** (Gade 1979).

The effective density deficit,

$$\Delta\rho_i^{\text{ef}}/\rho_o = \beta_S(S_a - S_i) - \beta_T(T_a - T_i^{\text{ef}}) \approx 0.024, \quad 6.$$

is slightly reduced but is still dominated by the effect of freshening. (This definition of ΔT_i^{ef} differs slightly from some literature, where it is related to the interfacial temperature; the magnitude of the latent heat makes the difference negligible.)

2.3. Melting

We refer to the phase change at the ice–water interface as melting, although it may be more proper to call it dissolving or ablating, since salt transport at the interface is important (Woods 1992, Kerr & McConnochie 2015). Most of the development of parameterizations for melting at a glacier–ocean interface has been by analogy with melting beneath sea ice, for which more observations are available (McPhee 2008). However, the extrapolation from an essentially horizontal interface in that setting to the sloping interface of ice shelves or glacier fronts is the subject of some uncertainty and current debate. Useful discussions are given by Holland & Jenkins (1999) and Jenkins et al. (2010).

2.3.1. Three-equation formulation. The ice–water interface is assumed to be in local thermodynamic equilibrium, so its temperature T_b and salinity S_b satisfy

$$T_b = T_L(S_b). \quad 7.$$

Heat and salt balances at the interface require that

$$\dot{m}[L + c_i(T_b - T_i)] = F_T, \quad \dot{m}(S_b - S_i) = F_S, \quad 8.$$

where \dot{m} is the melt rate (m/s), and F_T and F_S are the fluxes of heat and salt from the water to the interface. The terms proportional to c_i represent an approximation of the conductive heat flux from the interface into the ice. The heat balance can also be written in terms of the effective temperature defined in Equation 5; making use of the good approximation $T_b - T_L(S_i) \ll \tilde{L}/c$, it becomes $\dot{m}c(T_b - T_i^{\text{ef}}) = F_T$. If the heat and salt fluxes were known, Equations 7 and 8 together would determine the melt rate \dot{m} and the interfacial properties T_b and S_b .

The fluxes are usually related to temperature T and salinity S evaluated outside of interfacial boundary layers,

$$F_T = \gamma_T c(T - T_b), \quad F_S = \gamma_S(S - S_b), \quad 9.$$

where c is the heat capacity of the water, and γ_T and γ_S are transfer coefficients, having units of velocity. The most suitable form of these coefficients is not yet established. It is commonly assumed that they are proportional to the friction velocity, $U_* = \sqrt{\tau/\rho_o} = C_d^{1/2}U$, defined in terms of interfacial shear stress τ and related by a drag coefficient C_d to the velocity U (outside a viscous boundary layer). In that case, we write $\gamma_T = \Gamma_T U_*$ and $\gamma_S = \Gamma_S U_*$, or $\gamma_T = \text{St}_T U$ and $\gamma_S = \text{St}_S U$, where $\text{St}_T = C_d^{1/2} \Gamma_T$ and $\text{St}_S = C_d^{1/2} \Gamma_S$ are thermal and haline Stanton numbers (dimensionless heat transfer coefficients), which are assumed constant in most recent work (Jenkins et al. 2010). This constitutes the so-called three-equation formulation used in many models. It gives rise to a melt rate of the form $\dot{m} = MU$, where $M(T, S)$ is a melt rate coefficient depending on temperature and salinity (**Figure 2b**).

In the context of a subglacial plume, the velocity U is usually taken to be the plume velocity, but in some situations this has been supplemented or replaced by a background value to represent tidal currents, whose amplitude may be larger than the mean flow of the plume. Jenkins et al. (2010) suggest taking $U_*^2 = C_d(U^2 + U_{\text{tidal}}^2)$, where U_{tidal} is the root mean square of the tidal currents.

2.3.2. Two-equation formulation. An alternative description (McPhee et al. 2008) uses an approximate heat balance,

$$\dot{m}(L + c_i[T_L(S) - T_i]) = \text{St} U c [T - T_L(S)], \quad 10.$$

in which the interfacial temperature $T_b = T_L(S_b)$ is replaced by the freezing point of the water outside of the interfacial boundary layer $T_L(S)$, and a lumped Stanton number $\text{St} = C_d^{1/2} \Gamma_{TS}$ is adopted. This has been fitted to data from beneath the Ronne ice shelf and, at least with the limited constraints available, seems to work just as well as the seemingly more fundamental three-equation model (Jenkins et al. 2010).

Making the good approximation $T_L(S) - T_L(S_i) \ll \tilde{L}/c$, this melt rate can be expressed simply as a product of velocity and thermal driving $\Delta T = T - T_L(S)$,

$$\dot{m} = \text{St} U \frac{c \Delta T}{\tilde{L}}. \quad 11.$$

When expressed in terms of ΔT (rather than T) and S , the three-equation formulation also gives an approximately linear dependence on ΔT , with much weaker dependence on the salinity (**Figure 2b**). Equation 11 is therefore a useful simplification and is adopted in the plume models in Section 3.

2.3.3. Alternative formulations. The above parameterizations make the assumption that the velocity scale in the transfer coefficients is inherited, via the friction velocity, from the fluid velocity near the interface. An interpretation is that the width of the laminar sublayer, across which salt and heat must ultimately diffuse, is set by the shear stress exerted by fluid motion outside of the sublayer (Holland & Jenkins 1999, Wells & Worster 2008, McConnochie & Kerr 2017b). When the interface is sloped rather than horizontal, there is an alternative possibility that this width is set by the sublayer itself becoming buoyantly unstable. The lightest fluid is at the interface, so if that interface is sloped (and most obviously if it is vertical), the sublayer will be unstable to convection once its thickness δ exceeds a certain size. This can be interpreted as reaching a

LABORATORY EXPERIMENTS

There have been several experiments on the melting of vertical ice faces (Huppert & Turner 1980, Josberger & Martin 1981, Kerr & McConnochie 2015, Cenedese & Gatto 2016a). Due to size limitations, the experiments do not necessarily access the same turbulent regime that is thought to be relevant to large-scale geophysical flows. However, Kerr & McConnochie (2015) found good agreement with a uniform velocity-independent melt rate, $\dot{m} \propto \Delta T^{4/3}$. Experiments with an additional line source of buoyancy, and therefore higher velocities, hinted that the melt rate starts to scale with velocity (McConnochie & Kerr 2017a), possibly accessing the shear-driven boundary layer regime discussed in Section 2.3.3. In stratified water, Huppert & Turner (1980) and McConnochie & Kerr (2016a) found layered outflows, interpreted as double-diffusive behavior associated with different widths of thermal and solutal boundary layers. Experiments in a two-layer “ocean” with a point source of subglacial discharge (Cenedese & Gatto 2016a) showed that overall melting increases with the strength of the source, and that the plume may intrude both at the surface and at the density interface, in qualitative agreement with theoretical expectations and field observations.

Direct Numerical Simulations

Gayen et al. (2016) solved the Navier–Stokes equations for the turbulent flow at a vertical ice–water interface on a similar scale to that achieved in the laboratory. They found good agreement with the experiments of Kerr & McConnochie (2015), consistent with buoyancy controlling the width of the interfacial sublayer. Mondal et al. (2019) extended the computations to sloping interfaces.

critical value Ra_c of the local Rayleigh number $Ra = \Delta\rho_b g \delta^3 / \nu D_S$, where $\Delta\rho_b / \rho_o = \beta_S(S - S_b) - \beta_T(T - T_b)$ is the density difference across the sublayer. In that case, the transfer coefficients would be independent of the external fluid velocity and would scale with $1/\delta \propto \Delta\rho_b^{1/3}$. It can be shown (Kerr & McConnochie 2015) that one expects $\Delta\rho_b \propto \Delta T$, at least for small thermal driving, and the resulting melt rate therefore scales as $\dot{m} \propto \Delta T^{4/3}$, independent of velocity.

Wells & Worster (2008) developed a detailed model for a plume rising up a vertical wall, which suggests two transitions: first from a laminar state to a turbulent regime with sublayer width set by the buoyancy argument just given, and then to a second turbulent regime with sublayer width set by the shear stress of the turbulent outer flow, determined by a critical Reynolds number. The second transition occurs where the velocity is sufficiently large that the shear-driven criteria give a narrower sublayer (it can also be thought of in terms of a critical value of the Rayleigh number on the length scale of the plume). That study was for the simpler situation of a single component controlling buoyancy, but Kerr & McConnochie (2015) have suggested how the argument can be extended to the present case. McConnochie & Kerr (2017b) found that for a vertical interface, the transition to a shear-driven sublayer happens above a velocity of about 4 cm/s, and the velocity-dependent parameterizations described above may be appropriate in that case, at least in form (see the sidebar titled Laboratory Experiments).

2.4. Freezing

Freezing directly onto the ice–ocean interface can be described by the same heat and salt balances as in Equation 8. However, the melting and freezing processes are not symmetric (salt rejection produces denser water at the interface rather than lighter), and appropriate values of the transfer coefficients may therefore differ, perhaps significantly (McPhee et al. 2008). In the context of a subglacial plume, freezing is driven by upwelling water becoming supercooled due to the

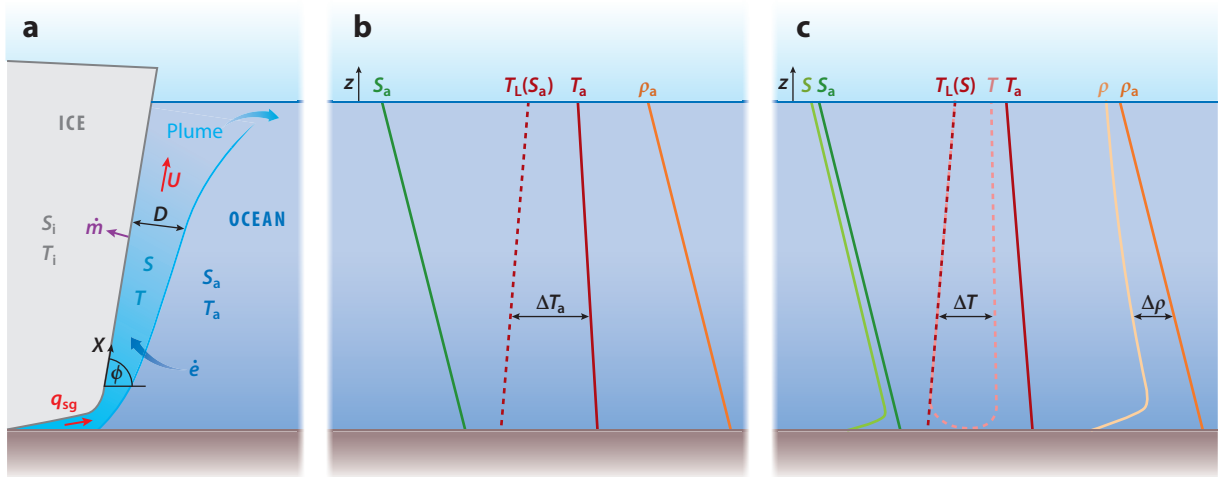


Figure 3

(a) A one-dimensional plume with velocity U , thickness D , salinity S , and temperature T . Also shown are subglacial discharge q_{sg} , submarine melt rate \dot{m} , entrainment rate \dot{e} , the ambient salinity S_a and temperature T_a , and the salinity S_i and temperature T_i of the ice. (b) Typical profiles of ambient salinity S_a , liquidus $T_L(S_a)$, temperature T_a , and density ρ_a together with ambient temperature excess ΔT_a . (c) Lighter colors show plume salinity S , temperature T , and density ρ .

depth-dependent freezing point. Such supercooling has the potential to produce frazil ice in suspension, so marine ice can grow by the precipitation of buoyant ice crystals, as well as freeze-on directly to the interface. This is discussed in Section 5.4.

3. ONE-DIMENSIONAL PLUMES

Some very useful insights and scaling arguments can be derived from simple one-dimensional models. These were originally developed for plumes beneath ice shelves by MacAyeal (1985) and Jenkins (1991), adapting earlier models of turbidity currents (e.g., Turner 1986). The framework described here follows most closely the work of Jenkins (2011) and Magorrian & Wells (2016).

The situation considered is shown in **Figure 3**. The coordinate X lies along the ice–ocean interface, with $\sin \phi = dz/dX$ being the local slope. Ultimately one would like to know the evolution of the ice–ocean interface, but the timescales over which this occurs are longer than those on which the plume evolves, allowing us to consider the steady-state behavior of the plume—and the resulting melt rates—for a given ice geometry. We mostly have in mind a vertical ice front ($\phi = \pi/2$), but the model is applicable to shallower slopes, too.

The plume is described in terms of its thickness D , average speed U , salinity S , and temperature T , for which top hat profiles are assumed (alternative shape factors are possible and would lead to similar equations with modified coefficients). Making a Boussinesq assumption, conservation equations for mass, momentum, salt, and heat are respectively

$$\frac{\partial}{\partial X}(DU) = \dot{e} + \dot{m}, \quad 12.$$

$$\frac{\partial}{\partial X}(DU^2) = D\Delta\rho g \sin \phi / \rho_o - C_d U^2, \quad 13.$$

$$\frac{\partial}{\partial X}(DUS) = \dot{e}S_a + \dot{m}S_i, \quad 14.$$

$$\frac{\partial}{\partial X}(DUT) = \dot{e}T_a + \dot{m}T_i^{\text{ef}}. \quad 15.$$

Here \dot{e} is the entrainment rate of ambient water and \dot{m} is the melt rate. The conventional entrainment assumption is $\dot{e} = EU$, where E is an entrainment coefficient. This depends on a competition between shear-induced turbulence and the stabilizing effect of mixing across a density interface (Ellison & Turner 1959, Turner 1986). A simple model is $E = E_0 \sin \phi$, where the inclusion of the slope attempts to account for this competition (Pedersen 1980), but alternative parameterizations dependent on Richardson number have also been used (e.g., Holland et al. 2007). The melt rate \dot{m} is given in terms of U , T , and S by one of the parameterizations described in Section 2.3.

The driving force due to buoyancy in Equation 13 can also have a component due to gradients in plume thickness, which allows the flow to become subcritical on shallow slopes. That term is neglected here because of the plume thickness being small. Turbulent wall drag is parameterized with the drag coefficient C_d , usually taken to have a value around 0.0025 (although there appears little observational constraint on this). The salinity and temperature equations have effectively been integrated across the ice–ocean boundary, making use of the flux boundary conditions of Equation 8.

The melt rate is found to be insignificant compared with the rate of entrainment and can reasonably be neglected in Equation 12, although it plays an important role in Equation 15 because the meltwater’s salinity and temperature deficit are large. Making that simplification, it is useful to rewrite the model in terms of density deficit $\Delta\rho$ and temperature excess ΔT ,

$$\frac{\partial}{\partial X}(DU) = EU, \quad 16.$$

$$\frac{\partial}{\partial X}(DU^2) = D\Delta\rho g \sin \phi / \rho_o - C_d U^2, \quad 17.$$

$$\frac{\partial}{\partial X}(DU \Delta\rho) = \dot{m} \Delta\rho_i^{\text{ef}} + \sin \phi \frac{d\rho_a}{dz} DU, \quad 18.$$

$$\frac{\partial}{\partial X}(DU \Delta T) = EU \Delta T_a + \dot{m} \Delta T_i^{\text{ef}} - \lambda \sin \phi DU. \quad 19.$$

We summarize some simple solutions to this model below. The effective meltwater buoyancy $\Delta\rho_i^{\text{ef}}$ and temperature excess ΔT_i^{ef} are essentially constants, given by Equations 5 and 6, respectively. The ambient thermal driving $\Delta T_a = T_a - T_L(S_a)$ will generally vary with depth; it is assumed known here, with initial value ΔT_{a0} . The final terms in Equations 18 and 19 account for ambient stratification and the depth dependence of the freezing point.

3.1. Plumes Driven by Subglacial Discharge

If the plume is fed by subglacial discharge (per unit width) q_{sg} , the most important driver is the initial buoyancy flux, $q_{\text{sg}} \Delta\rho_{\text{sg}}$. In some cases this may be sufficiently large that melting of the ice face (the first term on the right-hand side of Equation 18) has a negligible effect on buoyancy, and the plume dynamics are then decoupled from melting. The subglacial mass flux itself is usually insignificant compared to the entrained water mass, so the situation is essentially an ideal plume (Turner 1979), in which U and ΔT adjust rapidly from their inlet values.

3.1.1. Uniform ambient ocean. If the ambient conditions are uniform, the slope of the ice front is constant, and we neglect depth dependence of the freezing point, the solution has linearly increasing thickness, constant velocity and temperature excess, and decreasing buoyancy,

$$D = EX, \quad U = \left[\frac{q_{\text{sg}} \Delta \rho_{\text{sg}} g \sin \phi}{\rho_o (E + C_d)} \right]^{1/3}, \quad \Delta \rho = \Delta \rho_{\text{sg}} \frac{q_{\text{sg}}}{DU}, \quad \Delta T = \frac{E}{E + \text{St}} \Delta T_{a0}, \quad 20.$$

where in the final term we have made use of the melt rate parameterization of Equation 11 for which we have $\dot{m} = U \text{St} c \Delta T / \tilde{L}$. This implies a constant melt rate that varies linearly with the ambient thermal driving and with the one-third power of the subglacial discharge (Jenkins 2011),

$$\dot{m} \sim \frac{E \text{St}}{E + \text{St}} \frac{c \Delta T_{a0}}{\tilde{L}} \left[\frac{q_{\text{sg}} \Delta \rho_{\text{sg}} g \sin \phi}{\rho_o (E + C_d)} \right]^{1/3}. \quad 21.$$

This makes clear the combined influence of entrainment E (which controls how fast heat is transferred from ambient water to the plume) and Stanton number St (which controls how fast heat is transferred from plume to interface). Note that $C_d \ll E$ is likely for vertical ice faces, and wall drag could reasonably be neglected in that case. For shallower slopes, when entrainment is reduced, wall drag can be the dominant factor limiting plume velocity.

3.1.2. Linear stratification. The length scale over which the buoyancy flux is lost due to ambient stratification is (from balancing the first and last terms in Equation 18)

$$\ell_\rho = \frac{1}{\sin \phi} \left(\frac{E + C_d}{E} \right)^{1/2} \left[\frac{q_{\text{sg}} \Delta \rho_{\text{sg}} g \sin \phi}{\rho_o (E + C_d)} \right]^{1/3} \left| \frac{g}{\rho_o} \frac{d\rho_a}{dz} \right|^{-1/2}. \quad 22.$$

Inserting this length scale into the uniform ambient solution of Equation 20 defines scales for each of the variables, and the model can then be cast in dimensionless form by writing, for example, $X = \ell_\rho \hat{X}$, $D = E \ell_\rho \hat{D}(\hat{X})$, etc. The resulting scaled variables (with hats) satisfy

$$\frac{\partial}{\partial \hat{X}} (\hat{D} \hat{U}) = \hat{U}, \quad \frac{\partial}{\partial \hat{X}} (\hat{D} \hat{U}^2) = (1 + \hat{C}_d) \hat{D} \Delta \hat{\rho} - \hat{C}_d \hat{U}^2, \quad 23.$$

$$\frac{\partial}{\partial \hat{X}} (\hat{D} \hat{U} \Delta \hat{\rho}) = -\hat{D} \hat{U}, \quad \frac{\partial}{\partial \hat{X}} (\hat{D} \hat{U} \Delta \hat{T}) = (1 + \hat{\text{St}}) \hat{U} \Delta \hat{T}_a - \hat{\text{St}} \hat{m}, \quad 24.$$

with $\hat{C}_d = C_d/E$, $\hat{\text{St}} = \text{St}/E$, $\Delta \hat{T}_a = \Delta T_a / \Delta T_{a0}$, and $\hat{m} = \hat{U} \Delta \hat{T}$ for the melt rate parameterization of Equation 11. Solutions to this scaled model are shown in **Figure 4a**.

Of interest are the position $X_{\text{neg}} \approx 1.44 \ell_\rho$ at which the plume becomes negatively buoyant and the position $X_{\text{stop}} \approx 2.06 \ell_\rho$ at which it comes to rest (inertia enables it to continue beyond the height of negative buoyancy). The plume water is at that point denser than its surroundings and can be expected to intrude and sink to a neutral height somewhere between the heights corresponding to X_{stop} and X_{neg} (Magorrian & Wells 2016). The properties of this glacially modified water are a mix of the subglacial discharge and ambient water that has been entrained.

3.1.3. Two-layer stratification. In some cases, particularly in Greenland fjords, a two-layer uniform stratification may be a better approximation of the ambient conditions. In that case the solution of Equation 20 can be used for the lower layer, with the buoyancy $\Delta \rho$ undergoing a sudden decrease at the density interface by an amount equal to the ambient density change. If $\Delta \rho$ is subsequently negative, the plume will decelerate and after an overshoot can be expected to intrude along the density interface (Straneo & Cenedese 2015).

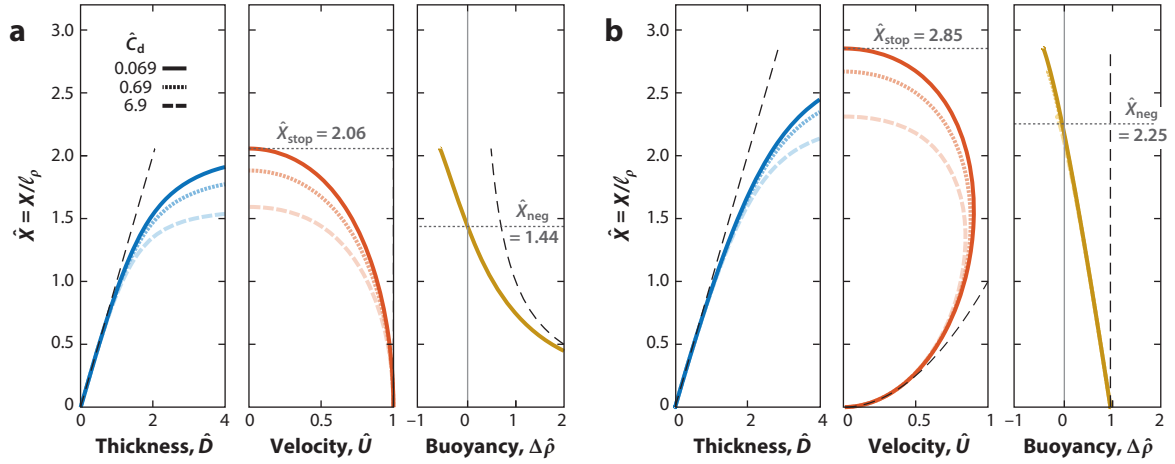


Figure 4

(a) Scaled solutions to Equations 23 and 24 for a subglacially driven plume with linear ambient stratification. Variable scales are given by inserting the length scale of Equation 22 into Equation 20. (b) Scaled solutions for a plume with no subglacial discharge and linear ambient stratification. Variable scales are given by inserting the length scale of Equation 29 into Equation 26. Both cases have $\Delta T_a = \Delta T_{a0}$. Values for the dimensionless drag coefficient \hat{C}_d are shown in the symbol key, with darker colors appropriate for a vertical slope and lighter colors for shallower slopes. Both solutions also have thermal driving $\Delta \hat{T} = 1$ and melt rate $\hat{m} = \hat{U} \Delta \hat{T}$. Black dashed lines show the unstratified solutions (Equations 20 and 26). Gray dotted lines indicate the locations \hat{X}_{neg} and \hat{X}_{stop} at which the plume becomes negatively buoyant and stops, respectively.

3.2. Plumes Driven by Submarine Melting

The buoyancy flux provided by submarine melting becomes more important than that provided by subglacial discharge after the length scale

$$\ell_{\text{sg}} = \frac{q_{\text{sg}} \Delta \rho_{\text{sg}}}{\dot{m} \Delta \rho_i^{\text{ef}}} = \left[\frac{\rho_o (E + C_d)}{g \sin \phi} \right]^{1/3} \left(\frac{E + \text{St}}{E \text{St}} \right) \frac{\tilde{L} \Delta \rho_{\text{sg}}^{2/3} q_{\text{sg}}^{2/3}}{c \Delta T_{a0} \Delta \rho_i^{\text{ef}}}. \quad 25.$$

This can vary substantially depending on the magnitude of subglacial discharge and the ambient temperature, but it obviously goes to zero for the limit $q_{\text{sg}} = 0$, which we now consider. For greater length scales, buoyancy comes from melting of the ice face and the dynamics are inherently tied to the thermodynamics. One can also expect these submarine melt-driven plumes to occur above the intrusion height of the subglacially driven plumes described in the previous section (in the less dense upper layer of Greenland fjords, for example).

3.2.1. Uniform ambient ocean. For uniform conditions, neglecting depth dependence of the freezing point and assuming the melt rate parameterization of Equation 11, the solution has increasing thickness and velocity, with constant buoyancy and temperature excess determined by a balance between entrainment and melting (Magorrian & Wells 2016),

$$D = \frac{2}{3} E X, \quad U = \left[\frac{E \Delta \rho g \sin \phi}{\rho_o (2E + \frac{3}{2} C_d)} \right]^{1/2} X^{1/2},$$

$$\Delta \rho = \frac{\text{St}}{E} \frac{c \Delta T}{\tilde{L}} \Delta \rho_i^{\text{ef}}, \quad \Delta T = \frac{E}{E + \text{St}} \Delta T_{a0}. \quad 26.$$

The corresponding melt rate increases with the square root of distance,

$$\dot{m} \sim \left(\frac{E \text{St}}{E + \text{St}} \frac{c \Delta T_{a0}}{\tilde{L}} \right)^{3/2} \left[\frac{\Delta \rho_i^{\text{ef}} g \sin \phi}{\rho_o (2E + \frac{3}{2} C_d)} \right]^{1/2} X^{1/2}. \quad 27.$$

The dependence on ambient thermal driving is stronger than for the subglacially dominated plume because of the feedback of melting on plume buoyancy and hence speed.

This solution is exact if there is no subglacial discharge. If there is subglacial discharge, there is a smooth transition from the behavior in Equation 21 for $X \ll \ell_{\text{sg}}$ to that in Equation 27 for $X \gg \ell_{\text{sg}}$. The melt rate always increases with distance during this transition and is always greater at any given position for larger subglacial discharge.

Note that because of the coupling between melting and buoyancy, this solution is only appropriate if the melt rate is proportional to plume velocity. If plume velocities are small, a different (e.g., tidal) velocity may control melting, as discussed in Section 2.3. If the melt rate is instead assumed constant, the appropriate solution is (McConnochie & Kerr 2016b)

$$D = \frac{3}{4} E X, \quad U = \left[\frac{\dot{m} \Delta \rho_i^{\text{ef}} g \sin \phi}{\rho_o (\frac{5}{4} E + C_d)} \right]^{1/3} X^{1/3}, \quad \Delta \rho = \frac{4}{3} \left[\frac{\rho_o (\frac{5}{4} E + C_d)}{\Delta \rho_i^{\text{ef}} g \sin \phi} \right]^{1/3} \frac{\dot{m}^{2/3} \Delta \rho_i^{\text{ef}}}{E X^{1/3}}. \quad 28.$$

3.2.2. Linear stratification. Returning to the solution in Equation 26, the ambient stratification becomes important on a length scale of

$$\ell_\rho = \frac{\text{St}}{E + \text{St}} \frac{c \Delta T_{a0}}{\tilde{L}} \frac{\Delta \rho_i^{\text{ef}}}{\sin \phi} \left| \frac{d\rho_a}{dz} \right|^{-1}, \quad 29.$$

over which the buoyancy is reduced. Inserting this length scale into Equation 26 determines suitable values with which to scale each of the variables in this case. Following the same procedure as earlier, this leads to a similar set of dimensionless equations that depends only on the ratios $\hat{C}_d = C_d/E$ and $\hat{\Delta T}_a = \Delta T_a/\Delta T_{a0}$. Solutions for uniform ambient temperature are shown in **Figure 4b**. The buoyancy falls off almost linearly, resulting in a decrease in velocity and hence melting. The plume becomes negatively buoyant at a distance $X_{\text{neg}} \approx 2.25 \ell_\rho$ and stops at a distance $X_{\text{stop}} \approx 2.85 \ell_\rho$ (these numerical values are specific to the value of \hat{C}_d , as seen in the figure). Magorrian & Wells (2016) suggested that another similar plume is initiated at X_{stop} , and one can expect a sequence of such plumes to develop, each intruding at successively greater heights and forming a layered structure that would presumably interfere with the ambient water column in a nontrivial way.

3.2.3. Depth dependence of the freezing point. The depth dependence of the freezing point becomes important on the length scale

$$\ell_T = \frac{\Delta T_{a0}}{\lambda \sin \phi}. \quad 30.$$

Inserting this length in Equation 26 to define variable scales produces another dimensionless model that depends only on $\hat{C}_d = C_d/E$, $\hat{\text{St}} = \text{St}/E$, and $\hat{\Delta T}_a = \Delta T_a/\Delta T_{a0}$ (reverting to the unstratified case). Solutions are shown in **Figure 5** for uniform ambient thermal driving. The temperature excess of the plume becomes negative after a distance X_{freeze} , causing supercooling and consequent freeze-on (negative \dot{m}). Freeze-on reduces the buoyancy, so the plume becomes negatively buoyant and then stops. Note that this model treats freeze-on simply as negative melting and ignores the role of frazil ice discussed in Section 5.4.

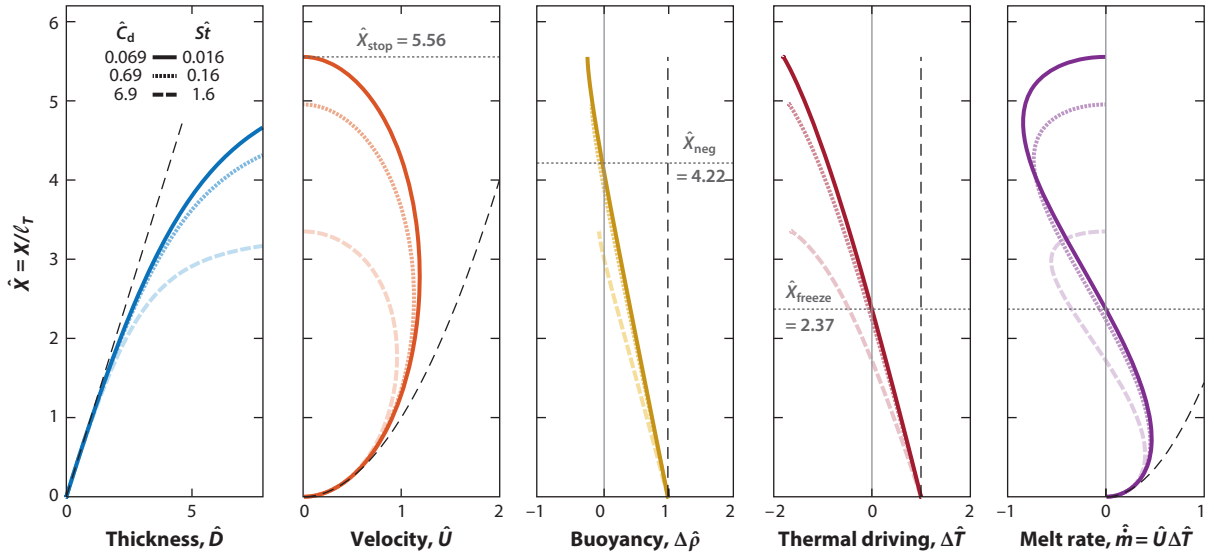


Figure 5

Scaled solutions for a plume with depth dependence of the freezing point, no subglacial discharge, and uniform ambient conditions with ambient thermal driving, $\Delta T_a = \Delta T_{a0}$. Values for the dimensionless drag coefficient \hat{C}_d and heat transfer coefficient \hat{St} are shown in the symbol key, with darker colors appropriate for a vertical slope and lighter colors for shallower slopes. Variable scales are given by inserting the length scale of Equation 30 into Equation 26. Black dashed lines show the solution not accounting for the freezing point change (Equation 26). Gray dotted lines indicate the locations \hat{X}_{freeze} , \hat{X}_{neg} , and \hat{X}_{stop} at which the plume begins to freeze, becomes negatively buoyant, and stops, respectively.

3.3. Point Sources of Subglacial Discharge

If subglacial discharge emerges from a channelized drainage system, it acts more like a point source than a line source. This gives rise to a plume that is more conical in shape, and a simple model is to treat such plumes as half of a classical axisymmetric plume (Kimura et al. 2014, Cowton et al. 2015, Slater et al. 2016). Direct numerical simulations of such a plume lend some support to this approach (Ezhova et al. 2018). With appropriate modifications to account for the area undergoing entrainment and the area in contact with the ice, and writing b for the radius of the half cone, the model is

$$\frac{\partial}{\partial X} \left(\frac{\pi}{2} b^2 U \right) = \alpha \pi b U, \quad \frac{\partial}{\partial X} \left(\frac{\pi}{2} b^2 U^2 \right) = \frac{\pi}{2} b^2 \Delta \rho g / \rho_o, \quad 31.$$

$$\frac{\partial}{\partial X} \left(\frac{\pi}{2} b^2 U \Delta \rho \right) = 2 b m \Delta \rho_i^{\text{ef}} + \frac{d \rho_a}{dz} \frac{\pi}{2} b^2 U, \quad \frac{\partial}{\partial X} \left(\frac{\pi}{2} b^2 U \Delta T \right) = \alpha \pi b U \Delta T_a. \quad 32.$$

The entrainment coefficient in this case is conventionally written as α . We have specialized to the case of a vertical ice front ($\phi = \pi/2$) and neglected both wall drag and the cooling effect of melting, which are unlikely to be significant in that case, as well as the depth dependence of the freezing point.

As for a line plume, the contribution of melting to buoyancy is initially insignificant, and the buoyancy flux is conserved from the source. Over this region the ideal plume has

$$b = \frac{6\alpha}{5} X, \quad U = \frac{5}{6\alpha} \left(\frac{9\alpha}{5\pi} \right)^{1/3} \frac{(Q_{\text{sg}} \Delta \rho_{\text{sg}} g)^{1/3}}{\rho_o^{1/3} X^{1/3}}, \quad \Delta \rho = \frac{Q_{\text{sg}} \Delta \rho_{\text{sg}}}{\frac{\pi}{2} b^2 U}, \quad \Delta T = \Delta T_{a0}, \quad 33.$$

where Q_{sg} is the volume flux of subglacial discharge. If the melt rate parameterization of Equation 11 is adopted, the total (volumetric) melt rate over a depth H is

$$\int_0^H 2bm \, dX \sim \frac{6}{5} \left(\frac{9\alpha}{5\pi} \right)^{1/3} \frac{\text{St} c \Delta T_{a0}}{\tilde{L}} \left(\frac{Q_{\text{sg}} \Delta \rho_{\text{sg}} g}{\rho_o} \right)^{1/3} H^{5/3}. \quad 34.$$

The melt rate again scales linearly with thermal driving and with the one-third power of the subglacial discharge.

For a localized source, it is more likely that the mass flux itself is significant too, and there may be an appreciable depth ℓ_0 over which the plume is dominated by the subglacial discharge. This can be accounted for using a virtual origin (Morton et al. 1956). The plume's velocity and thermal driving adjust over this scale, the latter increasing by dilution from its initial value of $\Delta T_{\text{sg}} \approx 0$ toward the ambient value of ΔT_{a0} . If ℓ_0 is a significant fraction of H , this cold region of the plume can weaken the dependence of melting on Q_{sg} (Slater et al. 2016). One can show that a linear stratification becomes important over a length scale of $\ell_\rho \propto Q_{\text{sg}}^{1/4} |\text{d}\rho_a/\text{d}z|^{-3/8}$, and the behavior of plumes reaching their level of neutral buoyancy can be analyzed as in Section 3.1 (Slater et al. 2016).

3.4. Melting Rates

The results of these models can be used to infer the sensitivity of melting to different parameters. Consider an example of a vertical ice front of width $W = 2$ km and depth $H = 500$ m, with uniform ambient water at thermal driving $\Delta T_{a0} = 4^\circ\text{C}$. If there is no subglacial discharge, the total (volumetric) melt rate from Equation 27 is expected to scale as

$$\int_0^H W \dot{m} \, dX \sim \frac{2^{1/2}}{3E^{1/2}} \left(\frac{\text{St} c \Delta T_{a0}}{\tilde{L}} \right)^{3/2} \left(\frac{\Delta \rho_i^{\text{ef}} g}{\rho_o} \right)^{1/2} H^{3/2} W \approx 4 \text{ m}^3/\text{s}, \quad 35.$$

with $\bar{m} \approx 0.3$ m/day. A point source plume fed by subglacial discharge $Q_{\text{sg}} = 100 \text{ m}^3/\text{s}$ would produce the total melt rate of Equation 34, around $1.2 \text{ m}^3/\text{s}$ ($\bar{m} \approx 0.1$ m/day), and if the same subglacial discharge were distributed over the width W , the melt rate from Equation 21 would be

$$\int_0^H W \dot{m} \, dX \sim \frac{1}{E^{1/3}} \frac{\text{St} c \Delta T_{a0}}{\tilde{L}} \left(\frac{Q_{\text{sg}} \Delta \rho_{\text{sg}} g}{\rho_o} \right)^{1/3} H W^{2/3} \approx 20 \text{ m}^3/\text{s}, \quad 36.$$

giving $\bar{m} \approx 1.7$ m/day. Total melting driven by the point source is relatively small compared with the background melting of the rest of the ice front and is dwarfed by the melting that would occur if the same subglacial discharge were distributed across the bed. Useful scalings with widths, depths, subglacial discharge, and thermal driving are derived from such expressions.

4. TWO-DIMENSIONAL PLUMES

Several studies have considered two-dimensional extensions of the model of Equations 12–15 to investigate flow in ice shelf cavities (e.g., Holland et al. 2007, Payne et al. 2007). Given the application to shallow slopes, these are posed in horizontal Cartesian coordinates (x, y). They consist of depth-integrated conservation equations (across the thickness of the plume), analogous to shallow-water-type models in other settings (e.g., Jungclaus & Backhaus 1994),

$$\frac{\partial D}{\partial t} + \nabla \cdot (D\mathbf{U}) = \dot{e} + \dot{m}, \quad 37.$$

$$\frac{\partial}{\partial t}(D\mathbf{U}) + \nabla \cdot (D\mathbf{U}\mathbf{U}) - fDV = \frac{\Delta\rho g D}{\rho_o} \frac{\partial d}{\partial x} - \frac{\partial}{\partial x} \left(\frac{\Delta\rho g D^2}{2\rho_o} \right) - C_d |\mathbf{U}|U + \nabla \cdot (vD\nabla U), \quad 38.$$

$$\frac{\partial}{\partial t}(DV) + \nabla \cdot (D\mathbf{U}V) + fDU = \frac{\Delta\rho g D}{\rho_o} \frac{\partial d}{\partial y} - \frac{\partial}{\partial y} \left(\frac{\Delta\rho g D^2}{2\rho_o} \right) - C_d |\mathbf{U}|V + \nabla \cdot (vD\nabla V), \quad 39.$$

$$\frac{\partial}{\partial t}(DS) + \nabla \cdot (D\mathbf{U}S) = \dot{e}S_a + \dot{m}S_i + \nabla \cdot (vD\nabla S), \quad 40.$$

$$\frac{\partial}{\partial t}(DT) + \nabla \cdot (D\mathbf{U}T) = \dot{e}T_a + \dot{m}T_i^{\text{ef}} + \nabla \cdot (vD\nabla T). \quad 41.$$

Here $\nabla = (\partial/\partial x, \partial/\partial y)$ is the horizontal divergence, $\mathbf{U} = (U, V)$ is the velocity, v is an eddy diffusivity, $d(x, y)$ is the elevation of the ice shelf base, and $f = 2\Omega \sin \varphi$ is the Coriolis parameter, with φ being the latitude. Parameterizations of entrainment $\dot{e} = E|\mathbf{U}|$ and melt rate \dot{m} are also required.

4.1. The Effects of Rotation

The key feature of Equations 37–41 that was ignored in the one-dimensional models is the Coriolis force. On larger scales this is significant, and the dominant force balance in Equations 38 and 39 is geostrophic, between the final terms on the left-hand side and the first terms on the right. The plume flows predominantly across the slope (to the left in the Southern hemisphere) rather than up it. Similar effects occur for katabatic winds (Van den Broeke & Van Lipzig 2003, Stiprski et al. 2007).

To illustrate the effect, **Figure 6** shows a plume beneath a linearly sloping ice shelf with uniform ambient conditions and no subglacial discharge. Without rotation, this situation is described by the one-dimensional solution of Equation 26, in which the plume had constant buoyancy $\Delta\rho$ and temperature excess ΔT . The plume thickness D grows linearly with x , and the dominant force balance between buoyancy and wall drag causes the velocity to increase as $U \sim (\Delta\rho g \sin \phi / \rho_o C_d)^{1/2} D^{1/2}$

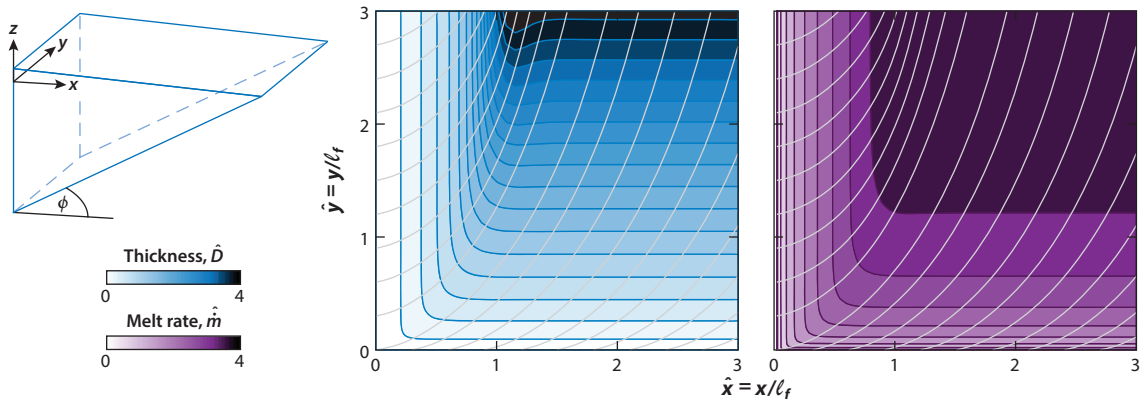


Figure 6

Solution for plume thickness \hat{D} , melt rate \hat{m} , and streamlines for a linearly sloping ice shelf with uniform ambient conditions, showing the effect of the Coriolis force ($f < 0$). These are steady solutions to Equations 37–41, ignoring the gradient of plume thickness and diffusion, with a melt rate given by Equation 11 and zero flux along $x = 0$ and $y = 0$. The solution is scaled using values in Equations 26 and 27, with $X = \ell_f$ the rotation length from Equation 42, and it depends upon the scaled drag coefficient $\hat{C}_d = 6.9$. For $\hat{x} \ll 1$, the solution is as for a one-dimensional plume (Equation 26). For $\hat{x}, \hat{y} \gg 1$, it asymptotes toward geostrophic balance (Equation 43).

($E \ll C_d$ is assumed here). The Coriolis term takes over from wall drag in balancing buoyancy once the plume is sufficiently thick, $D \sim C_d U/f$, which entails $D \sim C_d \Delta \rho g \sin \phi / \rho_o f^2$ (this scale is loosely equivalent to an Ekman layer depth). Since D is roughly $\frac{2}{3}Ex$, this defines a length scale of

$$\ell_f = \left(\frac{2E + \frac{3}{2}C_d}{E} \right) \frac{\Delta \rho g \sin \phi}{\rho_o f^2}, \quad 42.$$

over which the effects of rotation become important (the additional factor of $2E$ accounts for the possibility $E \sim C_d$). If the plume continues to thicken, drag becomes increasingly insignificant, and the plume tends toward a geostrophic balance with $U \ll V$ and

$$V = -\frac{\Delta \rho g \sin \phi}{\rho_o f}. \quad 43.$$

In this case, the plume is flowing across the slope and entrainment causes the thickness to increase in that direction rather than up the slope (**Figure 6**). Nevertheless, there is still a weak frictionally driven upslope component to the flow, analogous to that in a bottom Ekman layer. Clearly this leads to the collection of plume water at lateral boundaries, where topography then plays a key role in diverting the flow (e.g., Payne et al. 2007). The linear dependence of V on $\Delta \rho$, which is itself proportional to ΔT_a (Equation 26), suggests that melting should scale quadratically with thermal driving in this case (Holland et al. 2008).

The depth-integrated nature of these models means that they capture the competition between friction and geostrophy in a rather crude sense. In reality there must be significant vertical structure to the velocity (Wang et al. 2003, Cenedese et al. 2004), which could interact with the melt-induced stratification in a nontrivial way (Jenkins 2016). Understanding the structure of these large-scale plumes is an important area for future research.

4.2. Interaction with Ice Shelf Topography

Many ice shelves have channel-like features in their base (Rignot & Steffen 2008, Mankoff et al. 2012, Vaughan et al. 2012). These channels act as a topographical focus for subshelf plumes, with the possibility for enhanced melting and channel growth (Dutrieux et al. 2013, Alley et al. 2016), but also potentially reducing average melt rates by shielding other areas of the ice shelf (Millgate et al. 2013). The features may also act as zones of mechanical weakness that facilitate fracturing (Dow et al. 2018).

One mechanism for forming such channels is through a feedback between the evolution of ice shelf topography and plume-driven melting. This possibility has been studied with the two-dimensional model in Equations 37–41 (Gladish et al. 2012, Sergienko 2013, Dallaston et al. 2015). Although there appears to be no inherent instability of an initially uniform ice shelf, undulations in ice thickness inherited at the grounding line are found to grow downstream due to focused plume flow and melting. Lateral shear or nonuniform subglacial discharge can have the same effect. This is consistent with some observed channels that line up with expected locations of subglacial discharge (LeBrocq et al. 2013). Ice shelf channels are generally steeper on their western sides (Alley et al. 2016), consistent with the influence of the Coriolis force that causes enhanced flow and melting on their western flanks.

Detailed measurements have revealed that in some of these channels the ice shelf base is not smooth but comprises terraces that are hundreds of meters wide, separated by $\sim 45^\circ$ steps (Dutrieux et al. 2014). Melting is enhanced on the steep walls and varies from one terrace to another. It is currently unclear what mechanism lies behind these features.

5. FURTHER ISSUES

5.1. Interaction with Ambient Flow

In the simple models discussed above, the ambient ocean was assumed to be relatively motionless, with properties that are somehow known. In reality there are tidal and other currents, and the ambient properties are determined by the larger-scale ocean circulation, which is driven in part by the plume. In the simplest picture, upwelling plumes drive an overturning circulation, drawing in water at depth to replenish the outflowing glacially modified water. Such circulations appear to dominate some Greenland fjords (e.g., Gladish et al. 2015), but not ubiquitously. The presence of a sill can limit exchange with the continental shelf, and there are also tidal and wind-driven circulations (e.g., Jackson et al. 2014, Straneo & Cenedese 2015). In Antarctica, horizontal circulation plays a bigger role, and sea ice and wind forcing are significant in determining which water masses are drawn into the ice shelf cavities. A useful summary is provided by Jenkins et al. (2016).

5.2. Interaction with Ice Front Morphology and Calving

Plume models typically assume a vertical ice front, but real ice fronts have a more complicated geometry, partly due to nonuniform submarine melting (Fried et al. 2015). Slater et al. (2017a) coupled plume dynamics with an evolving ice front and found steady undercut profiles that depend on the magnitude of subglacial discharge. Undercutting of the ice front can facilitate fracturing and iceberg calving (e.g., O’Leary & Christoffersen 2013, Benn et al. 2017). This means that overall rates of frontal ablation (melting and calving combined) may be sensitive to the spatial pattern of melting, or perhaps its maximum, rather than necessarily the area average. Understanding the interplay of plume-driven melting with ice front evolution and calving is an important area for future research.

5.3. Detrainment

In the top hat models of Sections 3 and 4, one-way entrainment was assumed, and detrainment to the ambient effectively occurs at a point (X_{stop}) where the plume runs out of momentum and its thickness tends to infinity. Recent experimental studies have suggested that detrainment into a stratified ambient can be a more continuous process (Baines 2005, Cooper & Hunt 2010, Bonnebaigt et al. 2018), and that classical theories may need to be modified to account for this. Continuous detrainment is associated with a density variation across the plume, since denser fluid at the outer edge reaches neutral buoyancy earlier than the core. The situation appears to be exacerbated for a distributed buoyancy source, since lighter fluid is continually added to one side of the plume (Gladstone & Woods 2014). Hogg et al. (2017) developed a model with a linear buoyancy profile across the plume that allows for peeling detrainment. These studies raise the possibility that current models for submarine melt-driven plumes (including those in Sections 3.2 and 4) are not appropriate and need to be revised. This is again an important area for further work.

5.4. Frazil Ice

Frazil ice forms in plume water that is supercooled as a result of decompression. Suspended ice crystals increase buoyancy and can accelerate the plume, enhancing crystal growth, but larger crystals also precipitate more rapidly, thereby reducing the buoyancy. This leads to a complex interplay between nucleation, crystal growth, and plume dynamics. The effects were included in the plume model of Jenkins & Bombosch (1995). Smedsrud & Jenkins (2004) added multiple

OBSERVATIONS OF PLUMES

Surfacing plumes at tidewater glacier fronts have been observed with both time-lapse cameras and satellite imagery and have been used as indicators of subglacial discharge strength (e.g., Schild et al. 2016, Bartholomäus et al. 2016, Slater et al. 2017b). Several recent studies have sampled oceanographic properties of plume water close to the ice fronts (Mankoff et al. 2016, Stevens et al. 2016). Such measurements have allowed estimates of the amount of mixing with ambient water and of submarine melting. Comparison with plume theory suggests that some localized plumes may be better treated as finite-extent line plumes rather than point sources (Jackson et al. 2017), consistent with observations of large subglacial channel portals (Fried et al. 2015, Rignot et al. 2015).

In Antarctica, observations beneath the ice shelves are relatively limited. Oceanographic measurements have been made using autonomous underwater vehicles (Jenkins et al. 2010), but they are not able to sample the water immediately adjacent to the ice shelf base. Point measurements of the subshelf properties have been made by drilling down through the ice (e.g., Nicholls et al. 1997). Detailed measurements of ice shelf melting rates have been made using phase-sensitive radar (Corr et al. 2002), and broader-scale estimates of melting have been derived from satellite altimetry (e.g., Pritchard et al. 2012).

crystal size classes, Holland & Feltham (2006) extended it to two dimensions, and Rees Jones & Wells (2018) introduced a continuous size distribution. The main modification to the basic model of Equations 12–15 is to introduce the volume fraction of ice crystals C , which adds a term $(1 - \rho_i/\rho_o)C$ to the buoyancy in Equation 1. A conservation equation is included for the crystals, with freezing rate \dot{f} and precipitation (settling) rate \dot{p} , the latter of which adds to the thickness of the ice shelf along with the negative melting rate \dot{m} at the interface. The ice fraction C is broken down into a distribution over crystal size, and \dot{f} and \dot{p} are functionals of that distribution, whose form can have a large effect on the behavior of the plume (Smedsrud & Jenkins 2004, Rees Jones & Wells 2018).

5.5. Sediments

Subglacial discharge can transport significant quantities of glacially eroded sediment, which is deposited near the grounding line or ice front (e.g., Powell 1990, Drews et al. 2017). Suspended sediment is also a visible indicator of surfacing plumes (see the sidebar titled Observations of Plumes). Sediment concentrations vary considerably, but estimates of $C_s \sim 1\text{--}10\text{ kg/m}^3$ in larger subglacial channels are typical (e.g., Salcedo-Castro et al. 2013). The higher loads can provide a significant contribution to buoyancy, adding a term $(1/\rho_s - 1/\rho_o)C_s$ to Equation 1, but only in extreme cases ($C_s \gtrsim 40\text{ kg/m}^3$) would the subglacial discharge be negatively buoyant. The sediments are clay, silt, and sand, and their settling is complicated by flocculation of clay particles in sea water (e.g., Sutherland et al. 2015). Mugford & Dowdeswell (2011) developed a model of a sediment-laden subglacial plume to study deposition patterns, assuming negligible effect on buoyancy. The effect of particles on plume dynamics has also been studied in volcanic and other contexts (e.g., Sparks et al. 1991, Woods 2010).

6. NUMERICAL MODELING

6.1. Plume-Resolving Models

Several recent studies have used general circulation models (GCMs) to simulate plumes at a vertical ice front explicitly (e.g., Xu et al. 2012, 2013; Sciascia et al. 2013). Typical resolution is around 1–10 m near the ice front. Turbulence is described with an eddy diffusivity, whose size controls

the rate of entrainment and which is typically fitted to produce entrainment rates expected from plume theory. These studies have corroborated many results of the plume theories in Section 3.

Kimura et al. (2014) used a finite-element model to investigate subglacially driven plumes. An important finding was that the Coandă effect tends to keep the plume attached to the vertical ice face, even if initiated with significant horizontal momentum. They also found that overall melting increases if discharge is split between two channels, unless they are close enough for the plumes to merge, in which case melting is lower due to the reduced area of the affected ice face [a result also found in the laboratory experiments of Cenedese & Gatto (2016b)]. Slater et al. (2015) considered discharge from multiple point sources, finding that total melting increases if discharge is spread between more smaller channels, but that the associated plumes are less likely to reach the surface in a stratified environment. Again, this is consistent with the expectations derived from Section 3.

6.2. Larger-Scale Models

For larger-scale simulations it may be unrealistic to resolve plumes that are on the order of 10 m thick. Cowton et al. (2015) developed a subgrid parameterization for vertical plumes based on the model in Section 3.3, allowing GCM simulations of larger fjord systems over longer timescales (Carroll et al. 2017).

Simulations of the ocean beneath ice shelves are also performed using GCMs (e.g., Holland & Jenkins 2001, Holland et al. 2008, Losch 2008, Little et al. 2009). These models have varying numbers of vertical layers, and it is not always clear to what extent they resolve local dynamics near the ice shelf base. In some implementations, a dedicated mixed layer at the interface is used to parameterize the plume as well as the thermodynamic conditions at the interface. The mixed layer is treated similarly to Equations 37–41, although the implementation of entrainment and mixing is typically algorithm specific. The models do not generally include tides, so some form of parameterization of the tidal currents may also be necessary when considering subshelf melting rates (Makinson et al. 2011).

There are currently many efforts underway to develop coupled ice sheet–ocean simulations that are capable of evolving the ice shelf geometry and grounding line in response to melting (Dinniman et al. 2016, and references therein). Uncoupled glaciological models have made use of simplified and sometimes ad hoc parameterizations of subshelf melting (e.g., Pollard & DeConto 2012). Lazeroms et al. (2018) recently developed an improved parameterization based on the one-dimensional plume theory in Section 3.2.

SUMMARY POINTS

1. Subglacial plumes rise up the ice front and separate when they lose buoyancy in the stratified ocean. They entrain warm water that drives melting and control the properties of the glacially modified water that is exported to the open ocean.
2. Plumes driven by subglacial discharge are more vigorous and more easily observable. Submarine melting by such plumes is expected to scale linearly with thermal driving and to increase with both the magnitude and lateral extent of subglacial discharge.
3. Plumes driven only by submarine melting are generally weaker, and their dynamics more uncertain, due to the dependence on the melt rate, for which parameterizations are poorly constrained.
4. Upwelling plumes drive spatial patterns of melting that produce pronounced basal channels in ice shelves and promote undercutting and calving from ice fronts.

FUTURE ISSUES

1. Parameterizations of submarine melting are not well constrained. Field measurements, laboratory experiments, and numerical simulations could all help to elucidate the turbulent boundary layer structure and appropriate parameterizations.
2. More work is required to understand how plumes drive undercutting and calving at tide-water glaciers. An outstanding question is how ocean temperature, subglacial discharge, and ice dynamics combine to control overall frontal ablation rates.
3. Assumptions about the velocity and density structure of sub-ice shelf plumes are largely untested. Both observations and new theoretical insights could help to assess whether current models are adequate.

DISCLOSURE STATEMENT

The author is not aware of any biases that might be perceived as affecting the objectivity of this review.

ACKNOWLEDGMENTS

My thanks to Adrian Jenkins and Andrew Wells, from whom I have learnt most of what I know about this subject.

LITERATURE CITED

- Alley KE, Scambos TA, Siegfried MR, Fricker HA. 2016. Impacts of warm water on Antarctic ice shelf stability through basal channel formation. *Nat. Geosci.* 9:290–93
- Baines PG. 2005. Mixing regimes for the flow of dense fluid down slopes into stratified environments. *J. Fluid Mech.* 538:245–67
- Bartholomaeus TC, Stearns LA, Sutherland DA, Shroyer EL, Nash JD, et al. 2016. Contrasts in the response of adjacent fjords and glaciers to ice-sheet surface melt in West Greenland. *Ann. Glaciol.* 57:25–38
- Benn DI, Åström J, Zwinger T, Todd J, Nick FM, et al. 2017. Melt-under-cutting and buoyancy-driven calving from tidewater glaciers: new insights from discrete element and continuum model simulations. *J. Glaciol.* 63:691–702
- Bonnebaigt R, Caulfield C, Linden P. 2018. Detrainment of plumes from vertically distributed sources. *Environ. Fluid Mech.* 18:3–25
- Carroll D, Sutherland DA, Hudson B, Moon T, Catania GA, et al. 2016. The impact of glacier geometry on meltwater plume structure and submarine melt in Greenland fjords. *Geophys. Res. Lett.* 43:9739–48
- Carroll D, Sutherland DA, Shroyer EL, Nash JD, Catania GA, Stearns LA. 2017. Subglacial discharge-driven renewal of tidewater glacier fjords. *J. Geophys. Res. Oceans* 122:6611–29
- Cenedese C, Gatto VM. 2016a. Impact of a localized source of subglacial discharge on the heat flux and submarine melting of a tidewater glacier: a laboratory study. *J. Phys. Oceanogr.* 46:3155–63
- Cenedese C, Gatto VM. 2016b. Impact of two plumes' interaction on submarine melting of tidewater glaciers: a laboratory study. *J. Phys. Oceanogr.* 46:361–67
- Cenedese C, Whitehead JA, Ascarelli T, Ohiwa M. 2004. A dense current flowing down a sloping bottom in a rotating fluid. *J. Phys. Oceanogr.* 34:188–203
- Chandler D, Wadham J, Lis G, Cowton T, Sole A, et al. 2013. Evolution of the subglacial drainage system beneath the Greenland Ice Sheet revealed by tracers. *Nat. Geosci.* 6:195–98
- Cooper P, Hunt GR. 2010. The ventilated filling box containing a vertically distributed source of buoyancy. *J. Fluid Mech.* 646:39–58

- Corr HF, Jenkins A, Nicholls KW, Doake C. 2002. Precise measurement of changes in ice-shelf thickness by phase-sensitive radar to determine basal melt rates. *Geophys. Res. Lett.* 29:73-1-73-4
- Cowton T, Slater D, Sole A, Goldberg D, Nienow P. 2015. Modeling the impact of glacial runoff on fjord circulation and submarine melt rate using a new subgrid-scale parameterization for glacial plumes. *J. Geophys. Res. Oceans* 120:796-812
- Cuffey K, Paterson WSB. 2010. *The Physics of Glaciers*. Burlington, MA: Butterworth-Heinemann. 4th ed.
- Dallaston M, Hewitt I, Wells A. 2015. Channelization of plumes beneath ice shelves. *J. Fluid Mech.* 785:109-34
- Dinniman MS, Asay-Davis XS, Galton-Fenzi BK, Holland PR, Jenkins A, Timmermann R. 2016. Modeling ice shelf/ocean interaction in Antarctica: a review. *Oceanography* 29:144-53
- Dow CF, Lee WS, Greenbaum JS, Greene CA, Blankenship DD, et al. 2018. Basal channels drive active surface hydrology and transverse ice shelf fracture. *Sci. Adv.* 4:eao7212
- Drews R, Pattyn F, Hewitt I, Ng F, Berger S, et al. 2017. Actively evolving subglacial conduits and eskers initiate ice shelf channels at an Antarctic grounding line. *Nat. Commun.* 8:15228
- Dutrieux P, Stewart C, Jenkins A, Nicholls KW, Corr HF, et al. 2014. Basal terraces on melting ice shelves. *Geophys. Res. Lett.* 41:5506-13
- Dutrieux P, Vaughan DG, Corr HF, Jenkins A, Holland PR, et al. 2013. Pine Island glacier ice shelf melt distributed at kilometre scales. *Cryosphere* 7:1543-55
- Ellison T, Turner J. 1959. Turbulent entrainment in stratified flows. *J. Fluid Mech.* 6:423-48
- Ezhova E, Cenedese C, Brandt L. 2018. Dynamics of three-dimensional turbulent wall plumes and implications for estimates of submarine glacier melting. *J. Phys. Oceanogr.* 48:1941-50
- Fountain AG, Walder JS. 1998. Water flow through temperate glaciers. *Rev. Geophys.* 36:299-328
- Fricker HA, Scambos T, Bindshadler R, Padman L. 2007. An active subglacial water system in West Antarctica mapped from space. *Science* 315:1544-48
- Fried MJ, Catania GA, Bartholomaeus TC, Duncan D, Davis M, et al. 2015. Distributed subglacial discharge drives significant submarine melt at a Greenland tidewater glacier. *Geophys. Res. Lett.* 42:9328-36
- Gade HG. 1979. Melting of ice in sea water: a primitive model with application to the Antarctic ice shelf and icebergs. *J. Phys. Oceanogr.* 9:189-98
- Gayen B, Griffiths RW, Kerr RC. 2016. Simulation of convection at a vertical ice face dissolving into saline water. *J. Fluid Mech.* 798:284-98
- Gladish CV, Holland DM, Holland P, Price SF. 2012. Ice-shelf basal channels in a coupled ice/ocean model. *J. Glaciol.* 58:1227-44
- Gladish CV, Holland DM, Rosing-Asvid A, Behrens JW, Boje J. 2015. Oceanic boundary conditions for Jakobshavn Glacier. Part I: variability and renewal of Ilulissat Icefjord waters, 2001-14. *J. Phys. Oceanogr.* 45:3-32
- Gladstone C, Woods AW. 2014. Detrainment from a turbulent plume produced by a vertical line source of buoyancy in a confined, ventilated space. *J. Fluid Mech.* 742:35-49
- Hogg CA, Dalziel SB, Huppert HE, Imberger J. 2017. Inclined gravity currents filling basins: the impact of peeling detrainment on transport and vertical structure. *J. Fluid Mech.* 820:400-23
- Holland DM, Jenkins A. 1999. Modeling thermodynamic ice-ocean interactions at the base of an ice shelf. *J. Phys. Oceanogr.* 29:1787-800
- Holland DM, Jenkins A. 2001. Adaptation of an isopycnic coordinate ocean model for the study of circulation beneath ice shelves. *Mon. Weather Rev.* 129:1905-27
- Holland DM, Thomas RH, De Young B, Ribergaard MH, Lyberth B. 2008. Acceleration of Jakobshavn Isbræ triggered by warm subsurface ocean waters. *Nat. Geosci.* 1:659-64
- Holland PR, Feltham DL. 2006. The effects of rotation and ice shelf topography on frazil-laden ice shelf water plumes. *J. Phys. Oceanogr.* 36:2312-27
- Holland PR, Feltham DL, Jenkins A. 2007. Ice Shelf Water plume flow beneath Filchner-Ronne Ice Shelf, Antarctica. *J. Geophys. Res. Oceans* 112:C05044
- Huppert HE, Turner JS. 1980. Ice blocks melting into a salinity gradient. *J. Fluid Mech.* 100:367-84
- Jackson RH, Shroyer EL, Nash JD, Sutherland DA, Carroll D, et al. 2017. Near-glacier surveying of a subglacial discharge plume: implications for plume parameterizations. *Geophys. Res. Lett.* 44:6886-94

- Jackson RH, Straneo F, Sutherland DA. 2014. Externally forced fluctuations in ocean temperature at Greenland glaciers in non-summer months. *Nat. Geosci.* 7:503–8
- Jacobs S, Helmer H, Doake C, Jenkins A, Frolich R. 1992. Melting of ice shelves and the mass balance of Antarctica. *J. Glaciol.* 38:375–87
- Jenkins A. 1991. A one-dimensional model of ice shelf-ocean interaction. *J. Geophys. Res.* 96:20671–77
- Jenkins A. 2011. Convection driven melting near the grounding lines of ice shelves and tidewater glaciers. *J. Phys. Oceanogr.* 41:2279–94
- Jenkins A. 2016. A simple model of the ice shelf–ocean boundary layer and current. *J. Phys. Oceanogr.* 46:1785–803
- Jenkins A, Bombosch A. 1995. Modeling the effects of frazil ice crystals on the dynamics and thermodynamics of ice shelf water plumes. *J. Geophys. Res. Oceans* 100:6967–81
- Jenkins A, Dutrieux P, Jacobs SS, McPhail SD, Perrett JR, et al. 2010. Observations beneath Pine Island Glacier in West Antarctica and implications for its retreat. *Nat. Geosci.* 3:468–72
- Jenkins A, Dutrieux P, Jacobs SS, Steig EJ, Gudmundsson GH, et al. 2016. Decadal ocean forcing and Antarctic ice sheet response: lessons from the Amundsen Sea. *Oceanography* 29:106–17
- Jenkins A, Nicholls K, Corr H. 2010. Observation and parameterization of ablation at the base of Ronne Ice Shelf. *J. Phys. Oceanogr.* 40:2298–312
- Josberger EG, Martin S. 1981. A laboratory and theoretical study of the boundary layer adjacent to a vertical melting ice wall in salt water. *J. Fluid Mech.* 111:439–73
- Joughin I, Alley R, Holland D. 2012. Ice-sheet response to oceanic forcing. *Science* 338:1172–78
- Jungclauss JH, Backhaus JO. 1994. Application of a transient reduced gravity plume model to the Denmark Strait Overflow. *J. Geophys. Res. Oceans* 99:12375–96
- Kerr RC, McConnochie CD. 2015. Dissolution of a vertical solid surface by turbulent compositional convection. *J. Fluid Mech.* 765:211–28
- Kimura S, Holland PR, Jenkins A, Piggott M. 2014. The effect of meltwater plumes on the melting of a vertical glacier face. *J. Phys. Oceanogr.* 44:3099–117
- Lazeroms WM, Jenkins A, Gudmundsson GH, Van De Wal RS. 2018. Modelling present-day basal melt rates for Antarctic ice shelves using a parametrization of buoyant meltwater plumes. *Cryosphere* 12:49–70
- LeBrocq A, Ross N, Griggs J, Bingham R, Corr H, et al. 2013. Evidence from ice shelves for channelized meltwater flow beneath the Antarctic Ice Sheet. *Nat. Geosci.* 6:945–48
- Lewis E, Perkin R. 1986. Ice pumps and their rates. *J. Geophys. Res. Oceans* 91:11756–62
- Little CM, Gnanadesikan A, Oppenheimer M. 2009. How ice shelf morphology controls basal melting. *J. Geophys. Res. Oceans* 114:C12007
- Losch M. 2008. Modeling ice shelf cavities in a z coordinate ocean general circulation model. *J. Geophys. Res. Oceans* 113:C08043
- MacAyeal DR. 1985. Evolution of tidally triggered meltwater plumes below ice shelves. *Oceanol. Antarct. Cont. Shelf* 43:133–43
- Magorrian SJ, Wells AJ. 2016. Turbulent plumes from a glacier terminus melting in a stratified ocean. *J. Geophys. Res. Oceans* 121:4670–96
- Makinson K, Holland PR, Jenkins A, Nicholls KW, Holland DM. 2011. Influence of tides on melting and freezing beneath Filchner–Ronne Ice Shelf, Antarctica. *Geophys. Res. Lett.* 38:L06601
- Mankoff KD, Jacobs SS, Tulaczyk SM, Stammerjohn SE. 2012. The role of Pine Island Glacier ice shelf basal channels in deep-water upwelling, polynyas and ocean circulation in Pine Island Bay, Antarctica. *Ann. Glaciol.* 53:123–28
- Mankoff KD, Straneo F, Cenedese C, Das SB, Richards CG, Singh H. 2016. Structure and dynamics of a subglacial discharge plume in a Greenlandic fjord. *J. Geophys. Res. Oceans* 121:8670–88
- McConnochie CD, Kerr RC. 2016a. The effect of a salinity gradient on the dissolution of a vertical ice face. *J. Fluid Mech.* 791:589–607
- McConnochie CD, Kerr RC. 2016b. The turbulent wall plume from a vertically distributed source of buoyancy. *J. Fluid Mech.* 787:237–53

- McConnochie CD, Kerr RC. 2017a. Enhanced ablation of a vertical ice wall due to an external freshwater plume. *J. Fluid Mech.* 810:429–47
- McConnochie CD, Kerr RC. 2017b. Testing a common ice-ocean parameterization with laboratory experiments. *J. Geophys. Res. Oceans* 122:5905–15
- McPhee M. 2008. *Air-Ice-Ocean Interaction: Turbulent Ocean Boundary Layer Exchange Processes*. New York: Springer-Verlag
- McPhee MG, Morison JH, Nilsen F. 2008. Revisiting heat and salt exchange at the ice-ocean interface: Ocean flux and modeling considerations. *J. Geophys. Res. Oceans* 113:C06014
- Meiburg E, Kneller B. 2010. Turbidity currents and their deposits. *Annu. Rev. Fluid Mech.* 42:135–56
- Millgate T, Holland PR, Jenkins A, Johnson HL. 2013. The effect of basal channels on oceanic ice-shelf melting. *J. Geophys. Res. Oceans* 118:6951–64
- Mondal M, Gayen B, Griffiths RW, Kerr RC. 2019. Ablation of sloping ice faces into polar seawater. *J. Fluid Mech.* 863:545–71
- Morton B, Taylor G, Turner J. 1956. Turbulent gravitational convection from maintained and instantaneous sources. *Proc. R. Soc. Lond. A* 234:1–23
- Mugford R, Dowdeswell J. 2011. Modeling glacial meltwater plume dynamics and sedimentation in high-latitude fjords. *J. Geophys. Res. Earth Surf.* 116:F01023
- Nicholls K, Makinson K, Johnson M. 1997. New oceanographic data from beneath Ronne ice shelf, Antarctica. *Geophys. Res. Lett.* 24:167–70
- O’Leary M, Christoffersen P. 2013. Calving on tidewater glaciers amplified by submarine frontal melting. *Cryosphere* 7:119–28
- Parker G, Fukushima Y, Pantin HM. 1986. Self-accelerating turbidity currents. *J. Fluid Mech.* 171:145–81
- Payne A, Holland P, Shepherd A, Rutt I, Jenkins A, Joughin I. 2007. Numerical modeling of ocean-ice interactions under Pine Island Bay’s ice shelf. *J. Geophys. Res. Oceans* 112:C10019
- Pedersen FB. 1980. Dense bottom currents in rotating ocean. *J. Hydraul. Div.* 106:1291–308
- Pollard D, DeConto R. 2012. Description of a hybrid ice sheet-shelf model, and application to Antarctica. *Geosci. Model Dev.* 5:1273–95
- Powell RD. 1990. Glacimarine processes at grounding-line fans and their growth to ice-contact deltas. *Geol. Soc. Lond. Spec. Publ.* 53:53–73
- Pritchard H, Ligtenberg S, Fricker H, Vaughan D, Van den Broeke M, Padman L. 2012. Antarctic ice-sheet loss driven by basal melting of ice shelves. *Nature* 484:502–6
- Rees Jones D, Wells A. 2018. Frazil-ice growth rate and dynamics in mixed layers and sub-ice-shelf plumes. *Cryosphere* 12:25–38
- Rignot E, Fenty I, Xu Y, Cai C, Kemp C. 2015. Undercutting of marine-terminating glaciers in West Greenland. *Geophys. Res. Lett.* 42:5909–17
- Rignot E, Steffen K. 2008. Channelized bottom melting and stability of floating ice shelves. *Geophys. Res. Lett.* 35:L02503
- Salcedo-Castro J, Bourgault D, Bentley SJ, deYoung B. 2013. Non-hydrostatic modeling of cohesive sediment transport associated with a subglacial buoyant jet in glacial fjords: a process-oriented approach. *Ocean Model.* 63:30–39
- Schild KM, Hawley RL, Morriss BF. 2016. Subglacial hydrology at Rink Isbræ, West Greenland inferred from sediment plume appearance. *Ann. Glaciol.* 57:118–27
- Sciascia R, Straneo F, Cenedese C, Heimbach P. 2013. Seasonal variability of submarine melt rate and circulation in an East Greenland fjord. *J. Geophys. Res. Oceans* 118:2492–506
- Sergienko O. 2013. Basal channels on ice shelves. *J. Geophys. Res. Earth Surf.* 118:1342–55
- Slater DA, Goldberg DN, Nienow PW, Cowton TR. 2016. Scalings for submarine melting at tidewater glaciers from buoyant plume theory. *J. Phys. Oceanogr.* 46:1839–55
- Slater DA, Nienow P, Cowton T, Goldberg D, Sole A. 2015. Effect of near-terminus subglacial hydrology on tidewater glacier submarine melt rates. *Geophys. Res. Lett.* 42:2861–68
- Slater DA, Nienow P, Goldberg D, Cowton T, Sole A. 2017a. A model for tidewater glacier undercutting by submarine melting. *Geophys. Res. Lett.* 44:2360–68

- Slater DA, Nienow P, Sole A, Cowton T, Mottram R, et al. 2017b. Spatially distributed runoff at the grounding line of a large Greenlandic tidewater glacier inferred from plume modelling. *J. Glaciol.* 63:309–23
- Smedsrud LH, Jenkins A. 2004. Frazil ice formation in an ice shelf water plume. *J. Geophys. Res. Oceans* 109:C03025
- Sparks R, Carey S, Sigurdsson H. 1991. Sedimentation from gravity currents generated by turbulent plumes. *Sedimentology* 38:839–56
- Stearns LA, Smith BE, Hamilton GS. 2008. Increased flow speed on a large East Antarctic outlet glacier caused by subglacial floods. *Nat. Geosci.* 1:827–31
- Stevens LA, Straneo F, Das SB, Plueddemann AJ, Kukulya AL, Morlighem M. 2016. Linking glacially modified waters to catchment-scale subglacial discharge using autonomous underwater vehicle observations. *Cryosphere* 10:417–32
- Stiperski I, Kavčič I, Grisogono B, Durran DR. 2007. Including Coriolis effects in the Prandtl model for katabatic flow. *Q. J. R. Meteorol. Soc.* 133:101–6
- Straneo F, Cenedese C. 2015. The dynamics of Greenland's glacial fjords and their role in climate. *Annu. Rev. Mar. Sci.* 7:89–112
- Straneo F, Heimbach P. 2013. North Atlantic warming and the retreat of Greenland's outlet glaciers. *Nature* 504:36–43
- Straneo F, Sutherland DA, Holland D, Gladish C, Hamilton GS, et al. 2012. Characteristics of ocean waters reaching Greenland's glaciers. *Ann. Glaciol.* 53:202–10
- Sutherland BR, Barrett KJ, Gingras MK. 2015. Clay settling in fresh and salt water. *Environ. Fluid Mech.* 15:147–60
- Turner JS. 1979. *Buoyancy Effects in Fluids*. Cambridge, UK: Cambridge Univ. Press
- Turner JS. 1986. Turbulent entrainment: the development of the entrainment assumption, and its application to geophysical flows. *J. Fluid Mech.* 173:431–71
- Van den Broeke M, Van Lipzig N. 2003. Factors controlling the near-surface wind field in Antarctica. *Mon. Weather Rev.* 131:733–43
- Vaughan DG, Corr HF, Bindshadler RA, Dutrieux P, Gudmundsson GH, et al. 2012. Subglacial melt channels and fracture in the floating part of Pine Island Glacier, Antarctica. *J. Geophys. Res. Earth Surf.* 117:F03012
- Wang J, Ikeda M, Saucier FJ. 2003. A theoretical, two-layer, reduced-gravity model for descending dense water flow on continental shelves/slopes. *J. Geophys. Res. Oceans* 108:3161
- Wells A, Worster MG. 2008. A geophysical-scale model of vertical natural convection boundary layers. *J. Fluid Mech.* 609:111–37
- Woods AW. 1992. Melting and dissolving. *J. Fluid Mech.* 239:429–48
- Woods AW. 2010. Turbulent plumes in nature. *Annu. Rev. Fluid Mech.* 42:391–412
- Xu Y, Rignot E, Fenty I, Menemenlis D, Flexas MM. 2013. Subaqueous melting of Store Glacier, West Greenland from three-dimensional, high-resolution numerical modeling and ocean observations. *Geophys. Res. Lett.* 40:4648–53
- Xu Y, Rignot E, Menemenlis D, Koppes M. 2012. Numerical experiments on subaqueous melting of Greenland tidewater glaciers in response to ocean warming and enhanced subglacial discharge. *Ann. Glaciol.* 53:229–34



Contents

Anatol Roshko, 1923–2017 <i>Dimitri Papamoschou and Morteza Gharib</i>	1
David J. Benney: Nonlinear Wave and Instability Processes in Fluid Flows <i>T.R. Akylas</i>	21
Ocean Wave Interactions with Sea Ice: A Reappraisal <i>Vernon A. Squire</i>	37
Particles, Drops, and Bubbles Moving Across Sharp Interfaces and Stratified Layers <i>Jacques Magnaudet and Matthieu J. Mercier</i>	61
Convective Phenomena in Mushy Layers <i>Daniel M. Anderson and Peter Guba</i>	93
Shear Thickening of Concentrated Suspensions: Recent Developments and Relation to Other Phenomena <i>Jeffrey F. Morris</i>	121
Subglacial Plumes <i>Ian J. Hewitt</i>	145
Modeling Turbulent Flows in Porous Media <i>Brian D. Wood, Xiaoliang He, and Sourabh V. Apte</i>	171
Acoustic Tweezers for Particle and Fluid Micromanipulation <i>M. Baudoin and J.-L. Thomas</i>	205
Liquid-State Dewetting of Pulsed-Laser-Heated Nanoscale Metal Films and Other Geometries <i>Lou Kondic, Alejandro G. González, Javier A. Diez, Jason D. Fowlkes, and Philip Rack</i>	235
Capillarity in Soft Porous Solids <i>Jonghyun Ha and Ho-Young Kim</i>	263
Statics and Dynamics of Soft Wetting <i>Bruno Andreotti and Jacco H. Snoeijer</i>	285
Turbulence with Large Thermal and Compositional Density Variations <i>Daniel Livescu</i>	309

Patterns in Wall-Bounded Shear Flows <i>Laurette S. Tuckerman, Matthew Chantry, and Dwight Barkley</i>	343
Super-Resolution Imaging in Fluid Mechanics Using New Illumination Approaches <i>Minami Yoda</i>	369
Aeroacoustics of Silent Owl Flight <i>Justin W. Jaworski and N. Peake</i>	395
Immersed Methods for Fluid–Structure Interaction <i>Boyce E. Griffith and Neelesh A. Patankar</i>	421
Advances in Bioconvection <i>Martin A. Bees</i>	449
Machine Learning for Fluid Mechanics <i>Steven L. Brunton, Bernd R. Noack, and Petros Koumoutsakos</i>	477
Electroconvection near Electrochemical Interfaces: Experiments, Modeling, and Computation <i>Ali Mani and Karen May Wang</i>	509
Chemo-Hydrodynamic Patterns and Instabilities <i>A. De Wit</i>	531

Indexes

Cumulative Index of Contributing Authors, Volumes 1–52	557
Cumulative Index of Article Titles, Volumes 1–52	568

Errata

An online log of corrections to *Annual Review of Fluid Mechanics* articles may be found at <http://www.annualreviews.org/errata/fluid>